

# Transition Metal Oxide–Decorated Titanium Carbide MXene Electrodes for High-Energy Supercapacitors with an Expanded Potential Window

Sophy Mariam Varghese, Radhakrishnan Sheela Srihari, Moothaveetil Othayoth Anagha, and Raghavan Baby Rakhi\*

The growing demand for flexible and wearable devices drives the development of advanced energy-storage technologies.  $Ti_3C_2T_x$  MXene–based supercapacitors (SCs) gain attention for their fast charging and discharging capabilities, high power density, and long cycle life. However, the inherent restacking of MXene layers hinders efficient ion transport and limits electrochemical performance. To address this challenge, pseudocapacitive transition metal oxides (TMOs) such as CuO,  $Fe_3O_4$ , and  $MnO_2$  are introduced as spacers to enhance the electrochemical properties of  $Ti_3C_2T_x$  MXene electrodes. Among the composites, the  $Ti_3C_2T_x$  MXene– $MnO_2$  (MX–M) electrode exhibits a superior specific capacitance

of  $212\text{ F g}^{-1}$  (specific capacity of  $47\text{ mA h g}^{-1}$ ) at  $1\text{ A g}^{-1}$ , outperforming pure MXene and other composites in a 6M KOH electrolyte. The potential window of the symmetric coin-cell SC is successfully extended to 1.5 V in 1M  $LiClO_4/PC$  electrolyte, with the device delivering an impressive specific energy of  $19.4\text{ Wh kg}^{-1}$  at a specific power of  $1.5\text{ kW kg}^{-1}$ . Furthermore, by connecting three cells in series, the operating voltage is expanded to 4.5 V, demonstrating its effectiveness in powering light-emitting diodes. These findings highlight the potential of TMO-modified  $Ti_3C_2T_x$  MXene electrodes for next-generation energy-storage devices with enhanced electrochemical performance.

## 1. Introduction

In recent years, the global focus on energy storage has intensified due to growing concerns over fossil fuel depletion, population growth, and global warming, which have augmented the need for efficient energy and environmental solutions. The production and storage of renewable energy have thus become a critical challenge for scientists worldwide.<sup>[1,2]</sup> An ideal electrode material should efficiently deliver electric charge while rapidly accommodating high charge density. Energy-storage systems, including batteries and supercapacitors (SCs), play a crucial role in this domain. Among them, SCs stand out for their exceptional energy-storage capabilities. Their superior power density serves as a link between traditional dielectric capacitors and batteries, positioning them as a viable option for next-generation energy-storage applications. As a result, the quest for an efficient electrode material that caters to high-power devices stands at the forefront of advanced energy materials research. Exploring materials that possess active sites capable of facilitating both efficient electron transport and redox activity is crucial for improving

energy-storage capabilities.<sup>[3]</sup> One way to increase energy density is by using hybrid composite electrode materials with high specific capacitance.<sup>[4,5]</sup> In recent times, hybrid SCs have emerged innovative energy-storage solution, combining capacitor-type and battery-type electrode materials to leverage the best attributes of both technologies. However, achieving both high capacitance and power density in a single material or composite remains an ongoing challenge.<sup>[6–8]</sup> A wide range of carbon-based and 2D materials—such as transition metal compounds, phosphorene, and MXenes, have been extensively utilized to improve the electrochemical performance of SCs. Despite their potential, carbon-based materials often suffer from limitations like low capacitance and a restricted voltage window, which necessitates further exploration of advanced materials for better energy-storage performance. Graphene with outstanding physical and chemical properties have inspired researchers globally to explore various 2D materials for energy-storage applications. The discovery of MXene ( $Ti_3C_2T_x$ ) in 2011 marked a significant breakthrough, offering new possibilities for enhancing electrode material performance in energy-storage devices.<sup>[9]</sup>

MXenes, a family of metal carbides, nitrides, or carbonitrides have garnered considerable attention in recent years owing to their exceptional physicochemical characteristics, including high electrical conductivity, hydrophilicity, mechanical flexibility, and the presence of abundant surface functionalities. Among them,  $Ti_3C_2T_x$  MXene stands out for its outstanding capacitive behavior, as evidenced by nearly rectangular cyclic voltammograms (CVs) and symmetric galvanostatic charge–discharge (GCD) curves. This behavior stems from its ion-accessible layered structure, which support electric double-layer capacitance (EDLC), making it a highly promising candidate for energy-storage applications.<sup>[10]</sup>

S. M. Varghese, R. S. Srihari, M. O. Anagha, R. B. Rakhi

Centre for Sustainable Energy Technologies

CSIR-National Institute of Interdisciplinary Science and Technology (CSIR-NIIST)

Thiruvananthapuram, Kerala 695019, India

E-mail: rakhiraghavanbaby@niist.res.in

S. M. Varghese, R. S. Srihari, R. B. Rakhi

Academy of Scientific and Innovative Research (AcSIR)  
Ghaziabad 201002, India



Supporting information for this article is available on the WWW under <https://doi.org/10.1002/batt.202500304>

Despite the outstanding performance of titanium carbide MXenes, several challenges remain, such as limited capacitance, insufficient surface functional groups, unreacted microstructures, and restacking issues.<sup>[11]</sup> To address these limitations and further enhance the capacitance of MXene-based systems, researchers have explored the incorporation of materials such as polyaniline, reduced graphene oxide, conducting polymers, and other additives to improve their efficiency as electrode materials.<sup>[12–14]</sup> In recent studies, the energy-storage efficiency of MXene has been notably enhanced through its integration with transition metal oxides (TMOs), which offer excellent electrochemical energy-storage capabilities and multiple redox states.<sup>[15,16]</sup> Various metal oxides, including RuO<sub>2</sub>, MnO<sub>2</sub>, CuO, Fe<sub>3</sub>O<sub>4</sub>, V<sub>2</sub>O<sub>5</sub>, NiO, and Co<sub>3</sub>O<sub>4</sub>, have been widely investigated as potential electrode materials for SCs because of their excellent electrochemical characteristics. While RuO<sub>2</sub> is widely studied for its excellent pseudocapacitive behavior, its high-cost limits large-scale commercial applications. As a result, researchers are actively seeking cost-effective alternatives such as MnO<sub>2</sub>, CuO, Fe<sub>3</sub>O<sub>4</sub>, NiO, and V<sub>2</sub>O<sub>5</sub>. Among these, copper oxide (CuO), iron oxide (Fe<sub>3</sub>O<sub>4</sub>), and manganese dioxide (MnO<sub>2</sub>) are particularly attractive due to their abundance, affordability, nontoxic nature, ease of synthesis, and favorable electrochemical performance.

Metal oxides can be synthesized using various methods, including soft-chemical routes, sol-gel techniques, wet chemical methods, and hydrothermal processes. Among these, the hydrothermal method stands out for its simplicity, scalability, and ability to produce nanostructured materials with controlled morphology and size. Among the commonly studied metal oxides, manganese-based materials have garnered significant attention for pseudocapacitor applications due to their high theoretical capacitance ( $\approx 1370 \text{ F g}^{-1}$ ), good cycling stability, and elevated power density.<sup>[17]</sup> For instance, Wei et al. developed a novel 2D  $\beta$ -MnO<sub>2</sub> network with long-range order via a one-pot hydrothermal process, which demonstrated a specific capacitance of  $453 \text{ F g}^{-1}$  at a current density of  $0.5 \text{ A g}^{-1}$ .<sup>[18]</sup> However, the practical application of MnO<sub>2</sub> is often limited by its inherently low electrical conductivity and sluggish ion diffusion, which can lead to reduced specific capacitance, particularly at high current densities or during extended cycling.<sup>[19]</sup> To address these limitations, several strategies have been explored, including nanostructuring, transition metal doping, and the formation of composites with conductive materials.<sup>[20]</sup> In this context, MXene has emerged as a promising conductive scaffold due to its excellent electrical conductivity, 2D layered structure, and mechanical resilience. Integrating MnO<sub>2</sub> with MXene enhances charge transport, improves structural stability, and mitigates the drawbacks of pristine MnO<sub>2</sub>. The composite structure benefits from the insertion of redox-active metal oxides between MXene layers, which prevents restacking, increases surface area, and introduces additional pseudocapacitive behavior.<sup>[21]</sup> It is important to note that the objective of this study is not to exceed the theoretical capacitance of MnO<sub>2</sub>, but rather to overcome the intrinsic limitations of both components by creating a more robust and practically viable electrode architecture. The synergistic combination of MXene and MnO<sub>2</sub> facilitates improved charge-storage kinetics, enhanced structural integrity, and superior cycling stability,

paving the way for the development of high-performance SC devices. This performance can be further contextualized by comparing it with other MXene–metal oxide composites, such as MXene–CuO and MXene–Fe<sub>3</sub>O<sub>4</sub>, to gain deeper insights into the advantages of the MXene–MnO<sub>2</sub> system.

Anakha et al. synthesized CuO nanoparticles through a simple reduction method and integrated them onto MXene nanosheets. This composite exhibited an impressive specific capacitance and excellent long-term stability by retaining 86% of its initial capacitance after 10 000 cycles.<sup>[22]</sup> Wenyu Liang et al. developed an electrode composed of Ti<sub>3</sub>C<sub>2</sub>T<sub>x</sub>–Fe<sub>3</sub>O<sub>4</sub>-multiwalled carbon nanotubes (CNTs), achieving a specific capacitance of  $5.52 \text{ F cm}^{-2}$  within the negative potential range using a 0.5 M Na<sub>2</sub>SO<sub>4</sub> electrolyte.<sup>[23]</sup> Lu Zang et al. developed a high-performance electrode material by integrating Fe<sub>3</sub>O<sub>4</sub> nanoparticles onto Ti<sub>3</sub>C<sub>2</sub>T<sub>x</sub> using a simple in situ wet chemistry method within a solvothermal system. The resulting composite exhibited an impressive specific capacitance of  $368 \text{ F g}^{-1}$  and retained  $\approx 81\%$  of its initial capacitance after 10 000 charge–discharge cycles at a current density of  $10 \text{ A g}^{-1}$ .<sup>[24]</sup> Wang et al. reported the synthesis of d-Ti<sub>3</sub>C<sub>2</sub>T<sub>x</sub> and its composite with MnO<sub>2</sub>, highlighting its impressive electrochemical properties, including a capacitance of  $242 \text{ F g}^{-1}$  at  $1 \text{ A g}^{-1}$  and a remarkable retention rate of 97% after 5000 cycles of GCD.<sup>[25]</sup>

Tang et al. fabricated MXene nanosheets incorporated with MnO<sub>2</sub> particles, achieving a  $C_{sp}$  of  $130.5 \text{ F g}^{-1}$  at  $2 \text{ mV s}^{-1}$ , with cyclic stability of 95% maintained over 5000 cycles.<sup>[26]</sup> Additionally, Rakhi et al. synthesized  $\epsilon$ -MnO<sub>2</sub>/Ti<sub>2</sub>CT<sub>x</sub> and  $\epsilon$ -MnO<sub>2</sub>/Ti<sub>3</sub>C<sub>2</sub>T<sub>x</sub> using a direct chemical method, yielding a high capacitance of  $212 \text{ F g}^{-1}$  at  $1 \text{ A g}^{-1}$ , along with a notable energy density of  $12.25 \text{ Wh kg}^{-1}$  and a substantial power density of  $20 \text{ kW kg}^{-1}$ .<sup>[27]</sup>

Compared to bimetallic TMOs, single TMOs exhibit higher electrical conductivity, enhanced synergistic effects, and multiple-valence-state transitions. Metal oxides such as MnO<sub>2</sub>, Fe<sub>3</sub>O<sub>4</sub>, and CuO demonstrate exceptionally high pseudocapacitance compared to carbon-based materials, making them highly beneficial for enhancing energy density and improving the cycling stability of SCs. Among TMOs, MnO<sub>2</sub> stands out as an efficient electrode material for SCs due to its rapid charge–discharge capability, affordability, low toxicity, ease of fabrication, and environmental friendliness. Furthermore, its high theoretical specific capacitance and variable oxidation states, ranging from Mn<sup>3+</sup> to Mn<sup>4+</sup>, facilitate fast redox reactions, enhancing charge-storage efficiency compared to other materials.<sup>[28]</sup>

Building on the previous discussion, this work explores the synthesis and fabrication of symmetric SC electrodes using Ti<sub>3</sub>C<sub>2</sub>T<sub>x</sub> MXene–TMO composites, specifically Ti<sub>3</sub>C<sub>2</sub>T<sub>x</sub> MXene–CuO, Ti<sub>3</sub>C<sub>2</sub>T<sub>x</sub> MXene–Fe<sub>3</sub>O<sub>4</sub>, and Ti<sub>3</sub>C<sub>2</sub>T<sub>x</sub> MXene–MnO<sub>2</sub>, denoted as MX–C, MX–F, and MX–M, respectively. Among these, the best-performing MX–M is further utilized to fabricate a symmetric coin-cell SC, which successfully powers light-emitting diodes (LEDs), highlighting its potential for commercial applications.

## 2. Results and Discussions

Figure 1a,b presents a detailed schematic diagram illustrating the synthesis of Ti<sub>3</sub>C<sub>2</sub>T<sub>x</sub> MXene, the preparation of TMO-based

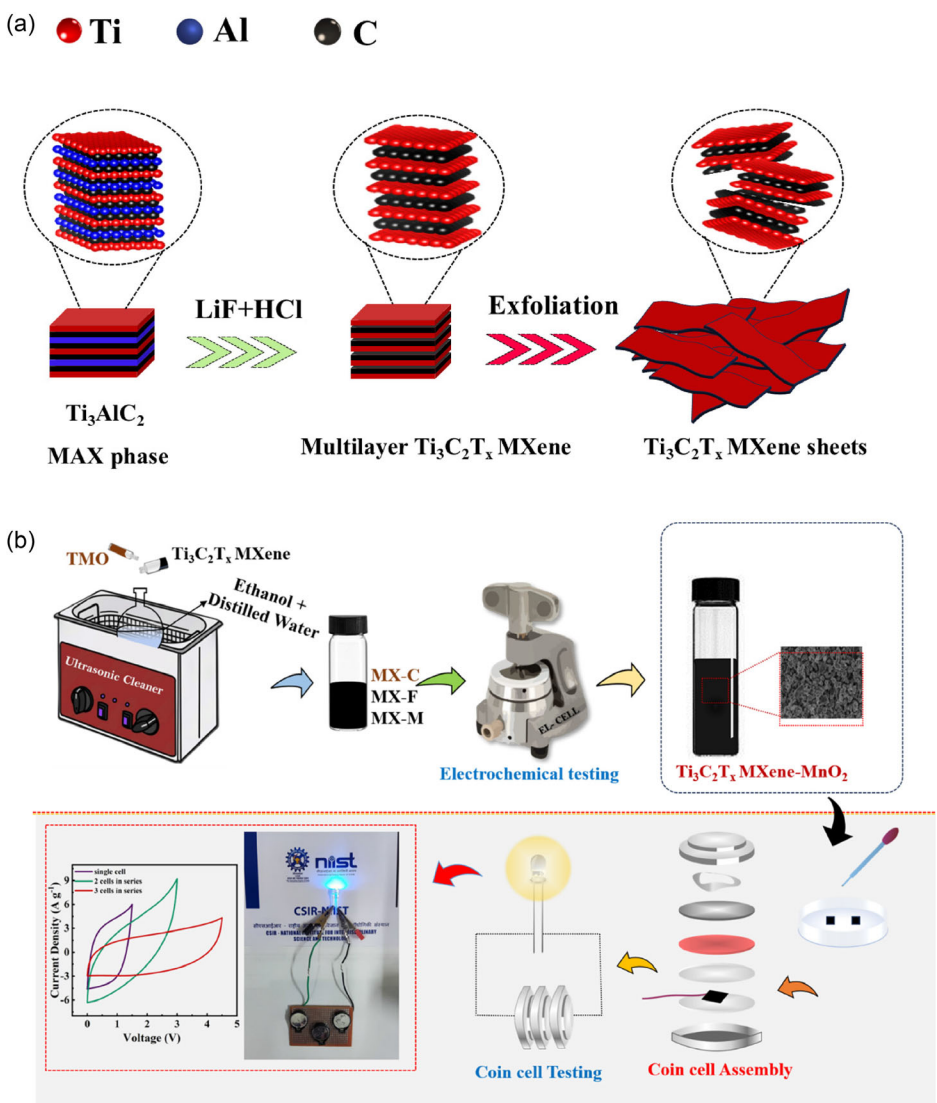


**Figure 1.** Schematic representation of a) the synthesis of  $\text{Ti}_3\text{C}_2\text{T}_x$  MXene nanosheets. b) Electrode fabrication, coin-cell assembly, and electrochemical testing of electrodes.

composites, the subsequent electrochemical analysis, and the fabrication of the device using the best-performing sample.  $\text{Ti}_3\text{C}_2\text{T}_x$  MXene nanosheets were successfully synthesized by extracting Al layers using an in situ Hydrofluoric acid (HF) etching method. In this process, LiF and HCl were used as the etching agents to eliminate the need for hazardous HF treatment. Moreover, the LiF/HCl approach facilitates easier delamination due to  $\text{Li}^+$  intercalation, which increases the d spacing, thereby enhancing ion diffusion and improving electrochemical performance.

The structural and phase analysis of the synthesized  $\text{Ti}_3\text{C}_2\text{T}_x$  MXene, along with  $\text{Ti}_3\text{C}_2\text{T}_x-\text{CuO}$  (MX-C),  $\text{Ti}_3\text{C}_2\text{T}_x-\text{Fe}_3\text{O}_4$  (MX-F), and  $\text{Ti}_3\text{C}_2\text{T}_x-\text{MnO}_2$  (MX-M) nanocomposites, was performed using X-ray diffraction (XRD), as shown in **Figure 2a**. The characteristic sharp Al (104) peak of  $\text{Ti}_3\text{AlC}_2$  was almost completely absent, confirming the successful formation of  $\text{Ti}_3\text{C}_2\text{T}_x$  MXene. Diffraction peaks at  $36.7^\circ$ , corresponding to the (103) planes, indicate the presence of  $\text{TiC}$  impurities.<sup>[29]</sup> All peaks were indexed

according to the standard  $\text{Ti}_3\text{AlC}_2$  pattern (ICDD No. 00-052-0875). Another notable feature in the  $\text{Ti}_3\text{C}_2\text{T}_x$  MXene spectra is the slight shift of peaks to lower angles, likely due to MXene's layered structure.<sup>[9]</sup> Additionally, a small quantity of  $\text{Ti}_3\text{C}_2(\text{OH})_2$  was observed in the XRD pattern around  $27.56^\circ$ , indexed to the (008) plane, formed during the MAX phase etching process.<sup>[30]</sup> The crystal structures of  $\text{Ti}_3\text{C}_2\text{T}_x$  MXene, CuO, and the  $\text{Ti}_3\text{C}_2\text{T}_x-\text{CuO}$  (MX-C) composite were characterized by XRD. For pure CuO, major peaks observed at  $2\theta$  values of  $32.65^\circ$ ,  $25.55^\circ$ ,  $38.85^\circ$ ,  $46.18^\circ$ ,  $46.38^\circ$ ,  $48.70^\circ$ ,  $53.43^\circ$ ,  $58.36^\circ$ ,  $61.63^\circ$ ,  $66.27^\circ$ ,  $68.01^\circ$ ,  $72.65^\circ$ , and  $75.17^\circ$  correspond to the (110), (-111), (111), (-112), (-202), (112), (020), (202), (-113), (-311), (220), (311), and (-222) planes, respectively. These diffraction peaks closely align with the standard CuO pattern as specified by the ICDD card no. 01-080-1268, confirming the successful synthesis of CuO (depicted in Figure S1a, Supporting Information). For MX-C composite, additional reflection peaks at  $18.16^\circ$  and  $27.43^\circ$  were identified, corresponding to the (004) and (008) planes of MXene

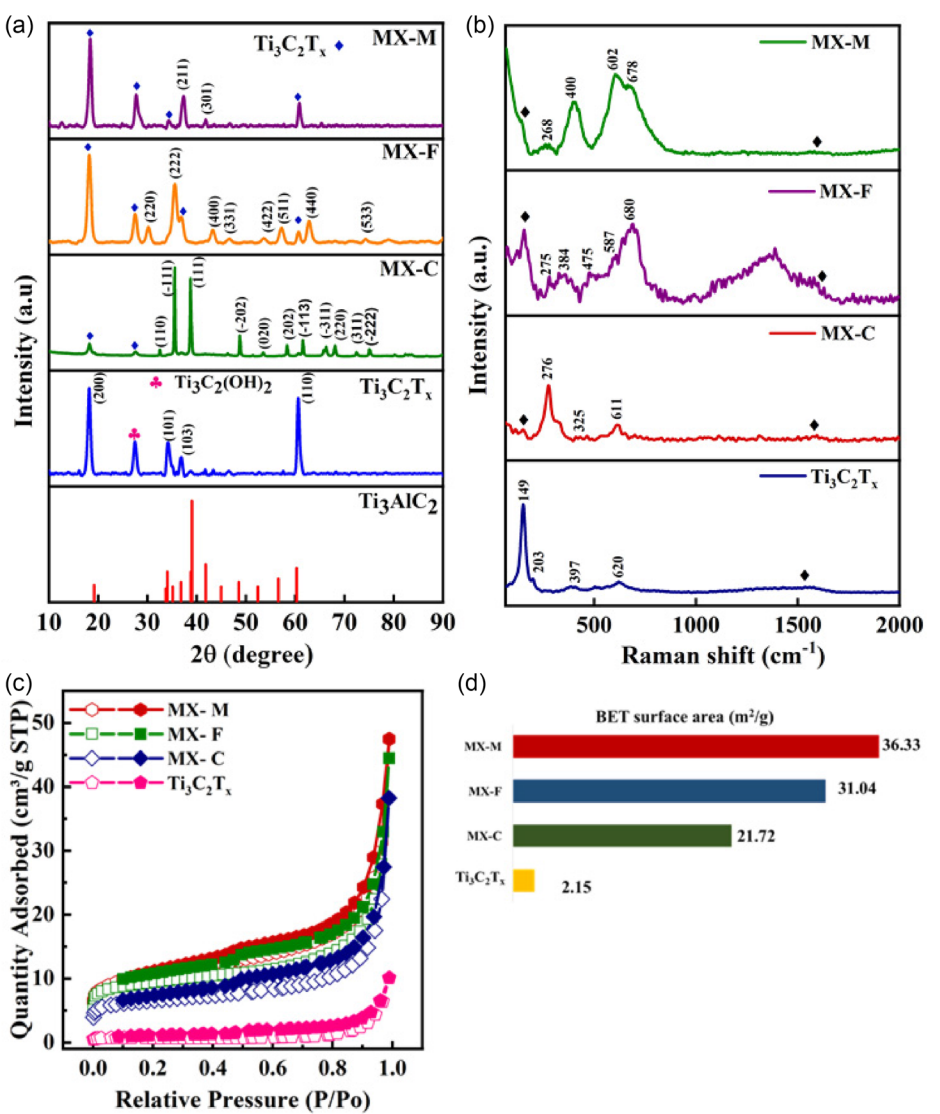


Figure 2. a) XRD spectra, b) Raman analysis, c) BET isotherms, and d) BET specific surface areas of MXene, MX-C, MX-F, and MX-M composites.

sheets. Notably, the characteristic CuO peaks in the composite show no significant shifts, indicating that the CuO nanoparticles are well integrated on the  $\text{Ti}_3\text{C}_2\text{Tx}$  MXene nanosheets without structural distortion. This confirms the successful *in situ* synthesis of CuO nanoparticles on  $\text{Ti}_3\text{C}_2\text{Tx}$  MXene layers. The XRD pattern in the figure illustrates the crystallographic analysis of  $\text{Ti}_3\text{C}_2\text{Tx}$  MXene,  $\text{Fe}_3\text{O}_4$ , and the  $\text{Ti}_3\text{C}_2\text{Tx}$  MXene– $\text{Fe}_3\text{O}_4$  (MX–F) nanocomposite. As shown in Figure S1b, Supporting Information, the synthesized  $\text{Fe}_3\text{O}_4$  exhibits eight distinct diffraction peaks at  $18.36^\circ$ ,  $30.15^\circ$ ,  $35.55^\circ$ ,  $43.08^\circ$ ,  $53.72^\circ$ ,  $57.20^\circ$ ,  $62.79^\circ$ , and  $74.39^\circ$ , corresponding to the (110), (−111), (111), (−112), (−202), (112), (020), (202), (−113), (−311), (220), (311), and (−222) planes of the cubic  $\text{Fe}_3\text{O}_4$  phase, as confirmed by the ICDD card no. 01-074-1910. The exclusive presence of  $\text{Fe}_3\text{O}_4$  peaks, without any additional diffraction signals, confirms the pure phase of  $\text{Fe}_3\text{O}_4$ .<sup>[31]</sup> In the XRD pattern of the MX–F composite, the peaks of both  $\text{Ti}_3\text{C}_2$  MXene and  $\text{Fe}_3\text{O}_4$  are present, with no new crystalline phases detected. This indicates that the composite is a physical mixture of  $\text{Fe}_3\text{O}_4$  nanoparticles and  $\text{Ti}_3\text{C}_2\text{Tx}$  MXene nanosheets

without any chemical transformation between the phases.<sup>[32]</sup> The XRD patterns of the  $\text{Ti}_3\text{C}_2\text{Tx}$  MXene– $\text{MnO}_2$  (MX–M) sample display additional broad peaks at  $\approx 2\theta$  values of  $12.56^\circ$ ,  $37.29^\circ$ , and  $41.92^\circ$ , corresponding to the (110), (211), and (301) reflections characteristic of tetragonal  $\alpha\text{-MnO}_2$ , as verified by the JCPDS card no. 00-044-0141<sup>[33]</sup> and the XRD pattern of bare  $\text{MnO}_2$  is shown in Figure S1c, Supporting Information. The peaks exhibit slight broadening, indicative of a low degree of crystallinity in the  $\alpha\text{-MnO}_2$  deposited on the  $\text{Ti}_3\text{C}_2\text{Tx}$  MXene sheets. Additionally, a subtle forward shift in the peaks is observed upon formation of the composite material, which can be attributed to an increase in *d* spacing and enhanced plane orderliness.<sup>[9]</sup>

Raman spectroscopy is a powerful tool for analyzing the structural characteristics of materials. Figure 2b presents the Raman spectra of the as-synthesized materials, providing detailed insights into their composition and quality. The Raman bands observed at  $149$ ,  $203$ ,  $397$ , and  $620 \text{ cm}^{-1}$ , located within the  $300$ – $800 \text{ cm}^{-1}$  range, are characteristic peaks of the  $\text{Ti}_3\text{C}_2\text{Tx}$  MXene.<sup>[34]</sup> The peak observed at  $203 \text{ cm}^{-1}$  is associated with

$A_{1g}$  symmetry, indicating out-of-plane vibrations of Ti atoms. In contrast, the bands at 397 and  $620\text{ cm}^{-1}$  correspond to  $E_g$  vibrations, representing in-plane (shear) movements of Ti, C, and surface functional group atoms.<sup>[35]</sup> The peak at  $397\text{ cm}^{-1}$  corresponds to in-plane vibrations involving Ti and C atoms within the plane, while the peak at  $620\text{ cm}^{-1}$  is associated with the  $E_{2g}$  mode, representing in-plane vibrations of C atoms. Additionally, the prominent peak at  $149\text{ cm}^{-1}$  is linked to the  $E_g$  mode of the  $\text{TiO}_2$  anatase phase, which may also contribute to the peaks observed at 397 and  $620\text{ cm}^{-1}$ .<sup>[36]</sup> The Raman spectrum of MX-C exhibits three peaks at 276, 325, and  $611\text{ cm}^{-1}$ . These peaks correspond to the  $A_g$ ,  $B_g^1$ , and  $B_g^2$  modes of CuO nanostructures.<sup>[37]</sup> Furthermore, the Raman spectrum of  $\text{Fe}_3\text{O}_4$  nanocrystals shows characteristic peaks at 275, 384, and  $475\text{ cm}^{-1}$ , attributed to the  $E_g$  mode, and a peak at  $587\text{ cm}^{-1}$  corresponding to the  $A_{1g}$  mode, confirming the presence of the  $\text{Fe}_3\text{O}_4$  phase.<sup>[31]</sup> Additionally, a Raman scattering peak at  $680\text{ cm}^{-1}$  is observed for  $\text{Fe}_3\text{O}_4$  nanoparticles, corresponding to the  $A_{1g}$  vibration mode.<sup>[38]</sup>

The Raman spectra of  $\text{MnO}_2$  exhibit prominent vibrational modes in the  $450$ – $760\text{ cm}^{-1}$  range, which are common features of most manganese oxides. These modes correspond to Mn–O stretching and bending vibrations arising from  $\text{Mn}^{4+}\text{O}_6$  octahedra. Specifically,  $\alpha\text{-MnO}_2$  shows two major peaks at 602 and  $678\text{ cm}^{-1}$ , primarily attributed to the stretching vibrations of  $\text{MnO}_6$  octahedra. At lower frequencies, Raman peaks correspond to the deformation modes of the Mn–O–Mn chains within the  $\text{MnO}_2$  octahedral lattice. In particular, the  $268\text{ cm}^{-1}$  band is associated with lattice vibrations and Mn–O bending modes, which arise from the  $\text{MnO}_6$  octahedral units and are observed across different  $\text{MnO}_2$  polymorphs.<sup>[39,40]</sup>

The  $\text{Ti}_3\text{C}_2\text{T}_x$  MXene and its composites were characterized using the Brunauer–Emmett–Teller (BET) method, with the corresponding isotherms and surface areas presented in Figure 2c,d. The BET surface area of MX-M was measured at  $36.33\text{ m}^2\text{ g}^{-1}$ , while  $\text{Ti}_3\text{C}_2\text{T}_x$  MXene, MX-C, and MX-F exhibited surface areas of  $31.04$ ,  $21.72$ , and  $2.15\text{ m}^2\text{ g}^{-1}$ , respectively. The isotherms closely resemble a Type IV isotherm (IUPAC classification), confirming the mesoporous nature of the samples. The BET surface area of the MX-M composite is significantly higher than that of pristine  $\text{Ti}_3\text{C}_2\text{T}_x$  MXene, likely due to the presence of metal oxide nanoparticles acting as interlayer spacers, which prevent the agglomeration or restacking of MXene sheet.<sup>[41]</sup> This improved structural configuration promotes greater exposure of electrochemically active sites and supports more efficient redox processes, while maintaining fast charge-transfer pathways through the conductive MXene framework, ultimately leading to enhanced electrochemical performance.

The microstructural characteristics of  $\text{Ti}_3\text{C}_2\text{T}_x$  MXene, MX-C, MX-F, and MX-M composites were analyzed using field-emission scanning electron microscope (FE-SEM) and transmission electron microscope (TEM), as shown in Figure 3a–h. As depicted in Figure 3a, the  $\text{Ti}_3\text{C}_2\text{T}_x$  MXene nanosheets exhibit a typical multilayered accordion-like structure.<sup>[42]</sup> In the MX-C composite (Figure 3b), CuO appears as rodlike flakes dispersed across the  $\text{Ti}_3\text{C}_2\text{T}_x$  MXene surface, indicating successful composite formation. In the MX-F composite (Figure 3c), the accordion-like

morphology is retained, with agglomerated  $\text{Fe}_3\text{O}_4$  nanoparticles distributed irregularly, either intercalated between layers or adsorbed on the surface. The MX-M composite (Figure 3d) combines MXene's layered structure with  $\text{MnO}_2$ 's stacked, interconnected flakes, where  $\text{MnO}_2$  nanoflowers cluster together, attaching to titanium carbide MXene nanosheets either decorating the surface or partially intercalating between layers. The FE-SEM images clearly demonstrate that metal oxide nanoparticles are distributed across both the  $\text{Ti}_3\text{C}_2\text{T}_x$  surfaces and interlayer spaces, confirming that the combination of sonication and stirring effectively produces well-decorated, delaminated  $\text{Ti}_3\text{C}_2\text{T}_x$  structures. This approach can also be extended to the hybridization of 2D materials with other metal oxide nanostructures.<sup>[43]</sup> The SEM images CuO,  $\text{Fe}_3\text{O}_4$ , and  $\text{MnO}_2$  are depicted in Figure S2, Supporting Information. The TEM results in Figure 3e–h further validate the findings from FE-SEM, confirming the successful integration of metal oxide nanoparticles onto the  $\text{Ti}_3\text{C}_2\text{T}_x$  MXene sheets, as well as their distribution across the surface and interlayer spaces.

The electrochemical performance of  $\text{Ti}_3\text{C}_2\text{T}_x$  MXene, MXene–CuO (MX-C), MXene– $\text{Fe}_3\text{O}_4$  (MX-F), and MXene– $\text{MnO}_2$  (MX-M) nanocomposites was investigated using CV, GCD, and electrochemical impedance spectroscopy (EIS). The CV curves of  $\text{Ti}_3\text{C}_2\text{T}_x$ , MX-C, MX-F, and MX-M at various scan rates are presented in Figure S3a–d, Supporting Information. These experiments were conducted in a two-electrode configuration in  $6\text{ M KOH}$  electrolyte over the range of  $5$  to  $200\text{ mV s}^{-1}$ . The results indicate a notable decrease in the specific capacitance of MXene electrodes at higher scan rates, which can be attributed to the instability and oxidation of Ti atoms on the MXene sheets.<sup>[44]</sup> The CV curves of MXene exhibit a nearly rectangular shape with no visible redox peaks, highlighting its pure EDLC behavior.<sup>[45]</sup> However, the incorporation of metal oxide nanoparticles alters this characteristic, likely due to the combined effects of MXene's EDLC properties and the pseudocapacitive contribution of TMOs.<sup>[46]</sup> Across all samples, ions are reversibly stored in the electrode, as indicated by the quasi-rectangular CV curves and nearly mirror-image current responses upon voltage reversal, particularly at high scan rates. For the MX-M sample, small reduction peaks are observed at lower scan rates, but they disappear as the scan rate increases, leading to a more pseudo-rectangular CV shape, as shown in the figures. These can be more clearly validated and distinguished through three-electrode measurements and the results are included in Supporting Information (Figure S4a–d, Supporting Information). The introduction of different metal oxides (Cu, Fe, Mn) significantly influences the specific capacitance values. A detailed analysis of the CV curves reveals that MX-M electrodes exhibit superior specific capacitance compared to other metal oxide composites. The incorporation of equal amounts of metal oxides between  $\text{Ti}_3\text{C}_2\text{T}_x$  MXene layers results in distinct electrochemical behaviors for each composite. A comparative evaluation of all samples highlights the superior performance of the MX-M electrode, as it exhibits the largest CV curve area, indicating the highest current response and optimal electrode-specific capacitance. This finding is further validated by the GCD curves, which were measured across a current density range of  $1$ – $5\text{ A g}^{-1}$  depicted in Figure S5a–d, Supporting Information, where the MX-M electrode exhibits the longest discharge time,

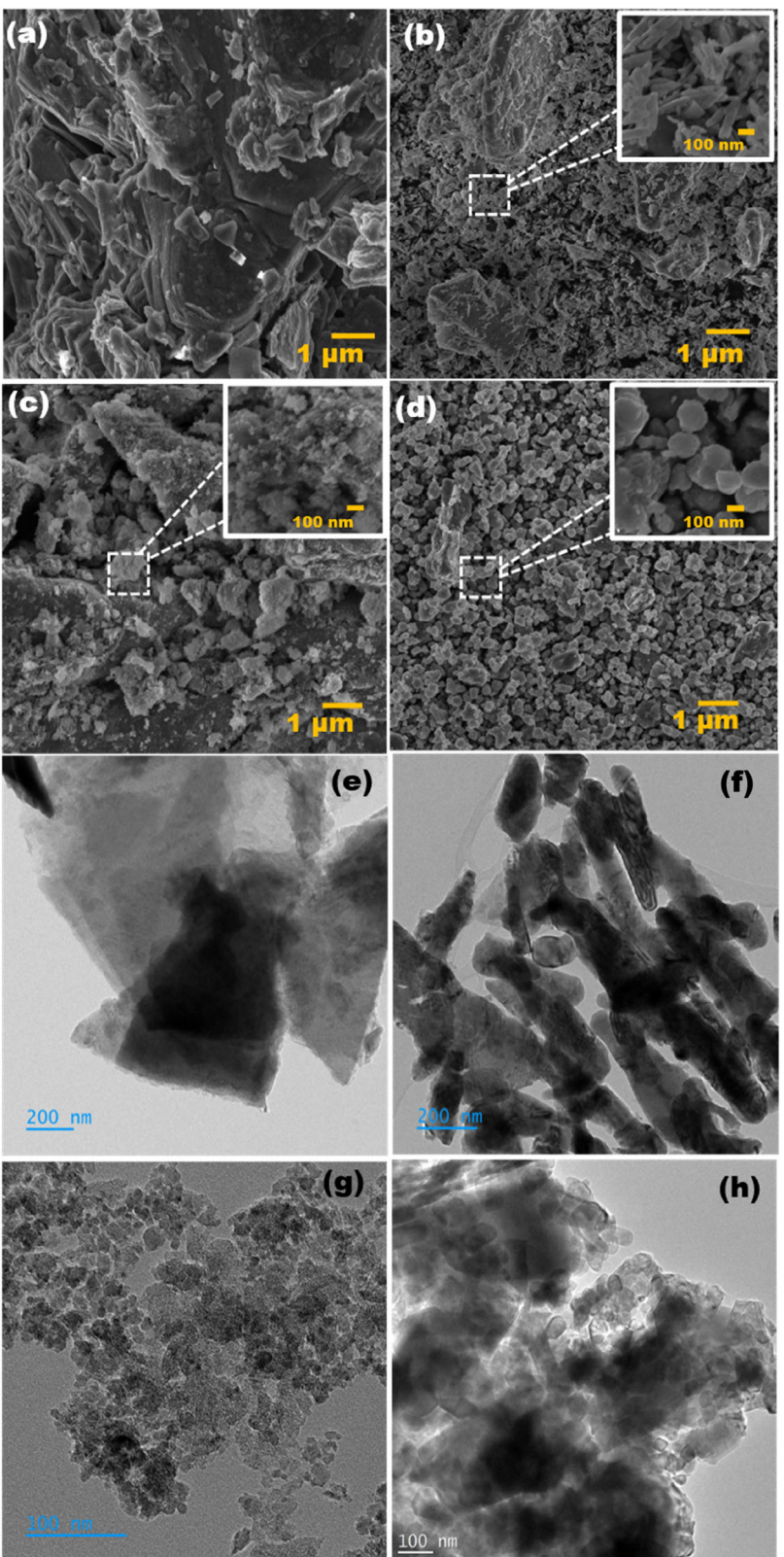


**Figure 3.** FE-SEM images - of a)  $\text{Ti}_3\text{C}_2\text{T}_x$  MXene, b) MX-C, c) MX-F, d) MX-M composites and TEM images of e)  $\text{Ti}_3\text{C}_2\text{T}_x$  MXene, f) MX-C, g) MX-F, and h) MX-M composites.

confirming its superior supercapacitive performance. The GCD curves also show an offset from the ideal triangular shape, confirming the contribution of pseudocapacitance. Among the tested

electrodes, MX-M demonstrates the best rate capability, further validating its potential for high-performance energy-storage applications.<sup>[47]</sup>

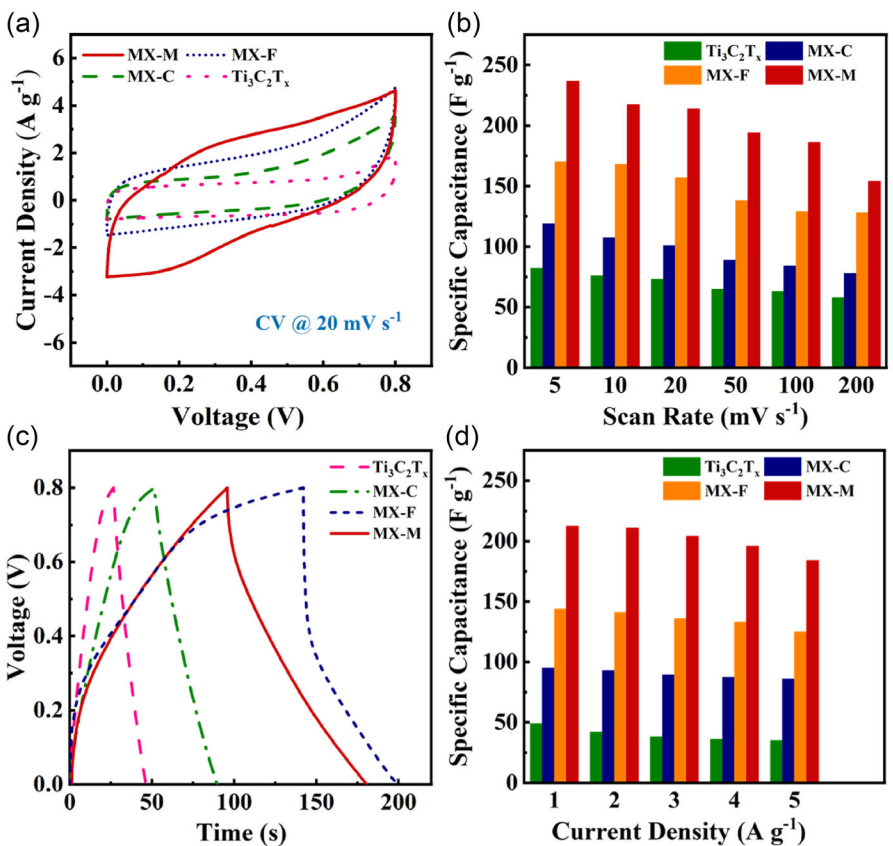


**Figure 4.** a) Cyclic voltammograms at 20 mV s<sup>-1</sup>. b) Specific capacitance variation as a function of scan rate. c) Galvanostatic charge–discharge curves at 1 A g<sup>-1</sup>. d) Specific capacitance variation as a function of current density for Ti<sub>3</sub>C<sub>2</sub>T<sub>x</sub> MXene, MX-C, MX-F, and MX-M electrodes.

Figure 4a present the comparison of the CV curves of Ti<sub>3</sub>C<sub>2</sub>T<sub>x</sub> MXene, MX-C, MX-F, and MX-M at 20 mV s<sup>-1</sup> and Figure 4c presents the comparison of the GCD profiles at 1 A g<sup>-1</sup>. This significant enhancement is primarily driven by the enhanced surface area and the pseudocapacitive nature of manganese oxide. For reference, the electrochemical responses of CuO, Fe<sub>3</sub>O<sub>4</sub>, and MnO<sub>2</sub> are illustrated in Figure S6, Supporting Information. The variations of specific capacitances with increasing scan rates and current densities were recorded in Figure 4b,d. As the scan rates and current densities increases, the C<sub>sp</sub> values decreases. At low scan rates, the slow accumulation of current allows electrolyte ions to penetrate deeper into the electrode's active surface, further maximizing ion accessibility and boosting the capacitive performance of the electrodes.<sup>[48]</sup> As the current density increases, the specific capacitance diminishes due to the incomplete reaction of the active material at higher charging rates. For current densities rising from 1 to 5 A g<sup>-1</sup>, the capacitance drops from 61 to 46 F g<sup>-1</sup> for Ti<sub>3</sub>C<sub>2</sub>T<sub>x</sub> MXene, 99 to 83 F g<sup>-1</sup> for MX-C, 143 to 124 F g<sup>-1</sup> for MX-F, and 212 to 188 F g<sup>-1</sup> for MX-M. This underscores the excellent rate capability of MX-M (89%) compared to Ti<sub>3</sub>C<sub>2</sub>T<sub>x</sub> MXene (75%), MX-C (84%), and MX-F (86%). The superior rate capability of MnO<sub>2</sub> in SCs, especially at higher scan rates, is primarily due to its faster redox kinetics and efficient ion diffusion. In contrast, other metal oxides often exhibit relatively poor ion diffusion and lower conductivity, which limit their charge-storage efficiency under similar conditions.<sup>[49,50]</sup>

It is important to correctly identify the dominant charge-storage mechanism and choose the appropriate metric specific capacitance (F g<sup>-1</sup>) for capacitive behavior or specific capacity (C g<sup>-1</sup> or mAh g<sup>-1</sup>) for diffusion-controlled or battery-type materials. While specific capacitance (F g<sup>-1</sup>) is used to report the performance of surface-dominated electrodes like Ti<sub>3</sub>C<sub>2</sub>T<sub>x</sub> MXene and pseudocapacitive composites, specific capacity (C g<sup>-1</sup> or mAh g<sup>-1</sup>) can also be considered for the composites, as they exhibit dominant faradaic charge-storage mechanisms due to the presence of redox-active metal oxides.<sup>[51]</sup>

In this study, the charge-storage mechanisms were further analyzed using cyclic voltammetry (CV). The b values, obtained from the power-law relationship  $i = a \cdot v^b$  (where  $i$  is the peak current and  $v$  is the scan rate), provide insight into the nature of the electrochemical process. A b value close to 1 indicates capacitive behavior, while a value near 0.5 suggests a diffusion-controlled mechanism. The calculated b values were 0.78 for Ti<sub>3</sub>C<sub>2</sub>T<sub>x</sub> (indicating a dominant capacitive response), and 0.52, 0.59, and 0.62 for MX-M, MX-C, and MX-F, respectively, confirming that the composite electrodes primarily store charge through diffusion-controlled processes. These results are presented in Figure S7, Supporting Information, which shows the linear fitting of log( $i$ ) versus log( $v$ ) to determine the b values. Furthermore, the specific capacity values of Ti<sub>3</sub>C<sub>2</sub>T<sub>x</sub> MXene and its metal oxide composites, derived from GCD analysis, are summarized in Table S1, Supporting Information for a more comprehensive comparison.

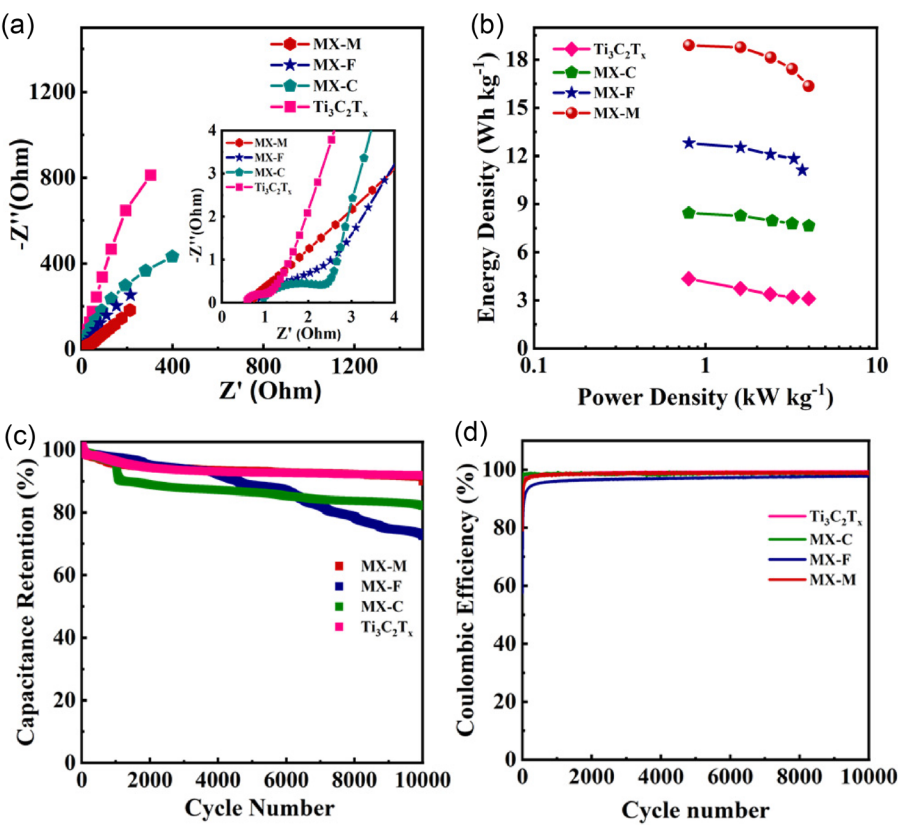


**Figure 5.** a) Nyquist plots, b) Ragone plots, and c,d) cyclic stability and Coulombic efficiency over 10 000 GCD cycles for Ti<sub>3</sub>C<sub>2</sub>T<sub>x</sub> MXene, MX-C, MX-F, and MX-M electrodes.

The charge-transfer resistance ( $R_{ct}$ ) is a key parameter for evaluating electrochemical performance and is therefore determined using EIS. To obtain the  $R_{ct}$  value, EIS were conducted over a frequency range from 0.1 Hz to 100 kHz. The Nyquist plots of Ti<sub>3</sub>C<sub>2</sub>T<sub>x</sub> MXene, MX-C, MX-F, and MX-M in Figure 5a illustrate characteristic semicircles in the high-frequency region and inclined Warburg lines in the low-frequency range, representing interfacial and diffusion resistances between the electrode and electrolyte.<sup>[52]</sup> The  $\times$  intercepts and semicircle diameters indicate that MX-M has lower solution and charge-transfer resistances than Ti<sub>3</sub>C<sub>2</sub>T<sub>x</sub> MXene, MX-C, and MX-F. This reduction in resistance is attributed to the MnO<sub>2</sub> structure and the conductive MXene network, which enhance electrolyte accessibility and facilitate internal charge transport within the electrode.<sup>[53]</sup> Moreover, the steeper Warburg slope of MX-M suggests improved ion diffusion properties. The relationship between energy density and power density is typically represented using a Ragone plot, as shown in Figure 5b. Among the samples, the MX-M composite demonstrated superior performance, achieving an energy density of 18.9 Wh kg<sup>-1</sup> at a power density of 801 W kg<sup>-1</sup>. In comparison, Ti<sub>3</sub>C<sub>2</sub>T<sub>x</sub> MXene, MX-C, and MX-F exhibited energy densities of 4.35, 8.4, and 12.8 Wh kg<sup>-1</sup> at power densities of 798, 799.5, and 800 W kg<sup>-1</sup>, respectively. Cyclic stability and Coulombic efficiency studies were conducted over 10 000 continuous GCD cycles for all materials and illustrated in Figure 5c,d. The capacitance retentions recorded were 92, 82, 70, and 90%, while the corresponding Coulombic efficiencies were calculated as 99.4, 98.3, 97.7, and 98.9%, for Ti<sub>3</sub>C<sub>2</sub>T<sub>x</sub> MXene, MX-C, MX-F, and MX-M, respectively.

and MX-M, respectively. The enhanced stability of the MX-M composite highlights the role of MnO<sub>2</sub> layers in preventing the stacking of MXene sheets. This structural improvement facilitates ion diffusion within the active material and increases surface accessibility to the electrolyte, thereby boosting performance. The MX-M composite's excellent structural integrity during cycling enables it to maintain capacitance over time. In contrast, MX-C and MX-F show noticeable capacitance degradation during charge-discharge cycles, leading to reduced long-term performance. It is well established that the electrochemical performance of SC materials is strongly influenced by their surface area, impacting both the electrochemical double-layer and pseudocapacitive storage mechanisms. The best performed sample MX-M exhibited the maximum surface area thus validates the obtained results. A detailed comparison table of previous literature reports on MXene–metal oxide-based SCs, highlighting performance benchmarks, is included in Table S2, Supporting Information, of the revised manuscript.<sup>[24,54–60]</sup>

The potential of the electrode as an SC device was demonstrated by fabricating a coin cell using the CR2032 type. Previous studies predominantly utilized aqueous electrolytes due to their high ionic conductivity and low internal resistance, which facilitate efficient ion penetration into active sites. However, the volatility and limited operational potential window of aqueous electrolytes restrict the energy density of such devices.<sup>[44]</sup> These limitations can be addressed by substituting aqueous KOH with an organic electrolyte, specifically 1 M lithium perchlorate in propylene carbonate (LiClO<sub>4</sub>/PC).

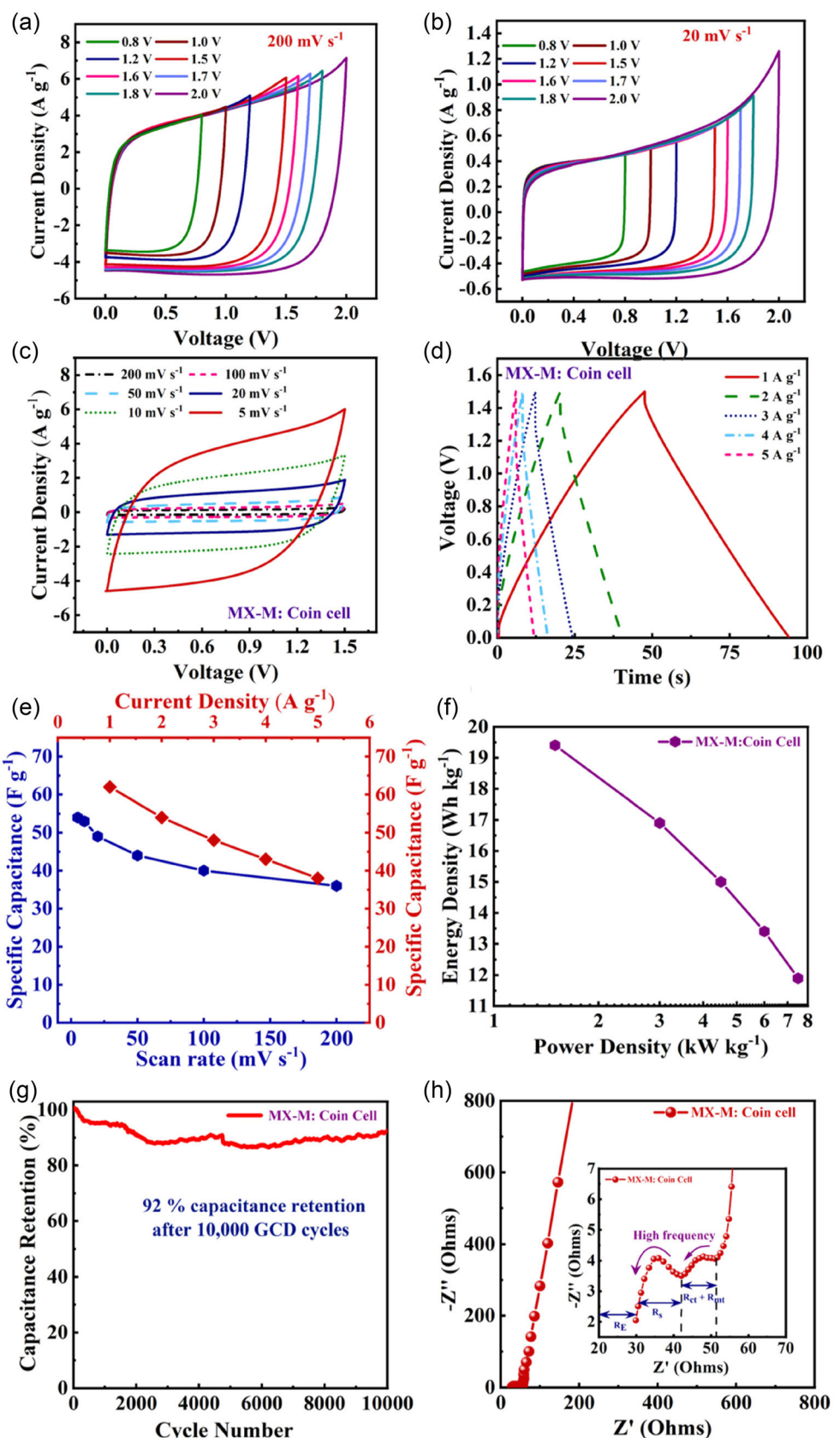


**Figure 6.** Electrochemical characteristics of MX-M coin-cell supercapacitors. a,b) CV curves at  $200$  and  $20 \text{ mV s}^{-1}$  in a different potential windows ranging from  $0.8$  to  $2 \text{ V}$ . c) cyclic voltammograms from  $5$  to  $200 \text{ mV s}^{-1}$  at a fixed operating voltage of  $1.5 \text{ V}$ . d) Galvanostatic charge–discharge from  $1$  to  $5 \text{ A g}^{-1}$ . e) Specific capacitance variation as a function of scan rate and current density. f) Ragone plots. g) Cyclic stability performance. h) Nyquist plots.

To evaluate device performance, the best-performing sample, MX-M, was selected as the electrode material in a standard EL cell with the 1 M LiClO<sub>4</sub>/PC electrolyte. Subsequently, a coin cell was fabricated using the same optimized electrode material. Electrochemical performance studies, including CV, GCD, and EIS, were conducted on the standard EL cell, as shown in Figure S8, Supporting Information. The use of the LiClO<sub>4</sub>/PC electrolyte extended the operational voltage from 0.8 to 1.5 V. Beyond 1.5 V, the electrode material deviated from ideal capacitive behavior.

The CV curves of the MX-M electrode, recorded at scan rates of 200 and 20 mV s<sup>-1</sup> within different potential windows ranging from 0.8 to 2 V, confirm this deviation (Figure 6a,b). As shown in Figure 6c, additional CV measurements were conducted from 5 to 200 mV s<sup>-1</sup> in a at a fixed operating voltage of 1.5 V, revealing a maximum specific capacitance of 54 F g<sup>-1</sup> at 5 mV s<sup>-1</sup>. The nearly rectangular shape of the CV curves, even at higher scan rates, highlights the excellent rate capability of the symmetric SC device. GCD tests were carried out from 1 to 5 A g<sup>-1</sup>, presented in Figure 6d with the device delivering a specific capacitance of 62 F g<sup>-1</sup> at 1 A g<sup>-1</sup>, which is consistent with previously reported values. The variations of specific capacitance with different scan rates and current densities are illustrated in the corresponding Figure 6e. A detailed examination of these curves reveals key characteristics, including a small voltage drop at the beginning of the discharge cycle. This drop can be attributed to the internal resistance of the electrodes.

EIS analysis was conducted to determine the electrolyte resistance ( $R_s$ ) and charge-transfer resistance ( $R_{ct}$ ) of the MX-M coin-cell

SC. The Nyquist plot (Figure 6h) and its inset showing the high-frequency region indicate  $R_s$  and  $R_{ct}$  values of 12.2 and 8.9 Ω, respectively. The cyclic stability test was conducted for the device and it showed an outstanding 92% capacitance retention even after continuous 10 000 GCD cycles and was shown in Figure 6g. The Ragone plot (Figure 6f) illustrates the energy and power density of the MX-M coin cell in the 1 M LiClO<sub>4</sub>/PC electrolyte. The device achieved a maximum energy density of 19.4 Wh kg<sup>-1</sup> and a power density of 1.5 kW kg<sup>-1</sup>. Notably, the energy density increased from 18.9 to 19.4 Wh kg<sup>-1</sup> as the voltage window extended to 1.5 V. Enhancing the applied potential range remains a key strategy for further improving the energy density of SC devices.

To deliver the desired combination of voltage and current, commercial SCs are often arranged in series, parallel, or a combination of both configurations. In this study, MX-M coin-cell SCs were fabricated by connecting three cells of identical mass in series (S) and parallel (P) configurations to enhance voltage and maximize current output, demonstrating the device's potential for real-world applications.

In the series configuration, the operating voltage increased as the number of cells increased, while the parallel configuration resulted in a significant increase in current density from 6.01 A g<sup>-1</sup> with a single cell to 68.7 A g<sup>-1</sup> with three cells connected in parallel. As shown in Figure 7a-d comparing a single cell, three cells in series (3S), and three cells in parallel configurations (3P), the 3S arrangement provided the highest operating voltage (4.5 V), while the 3P configuration delivered the highest current density.

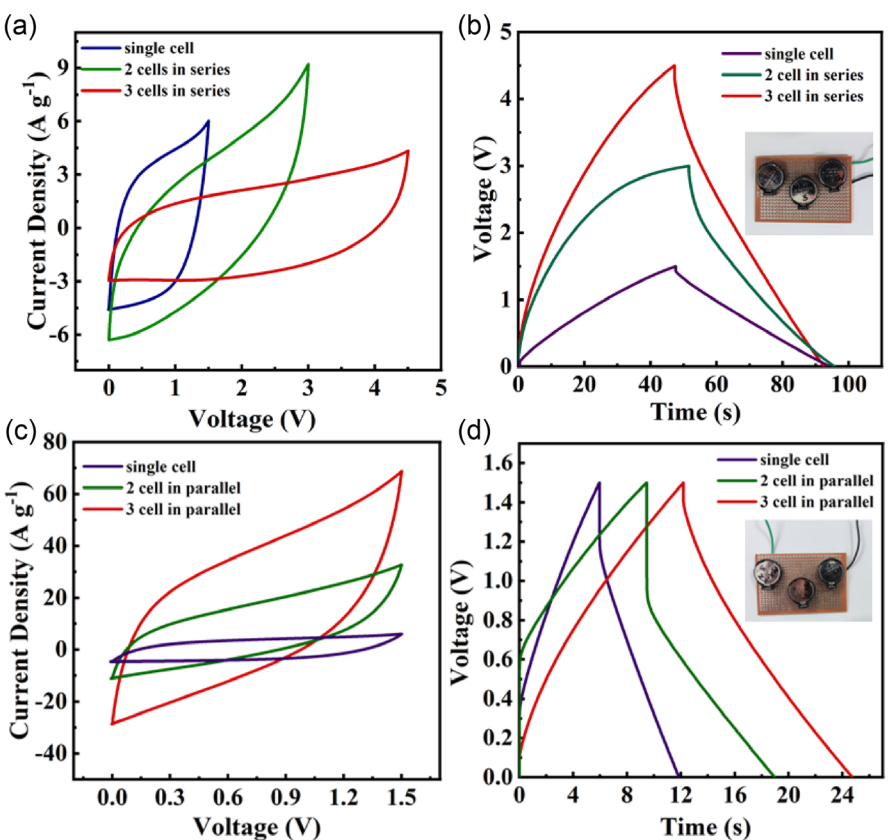
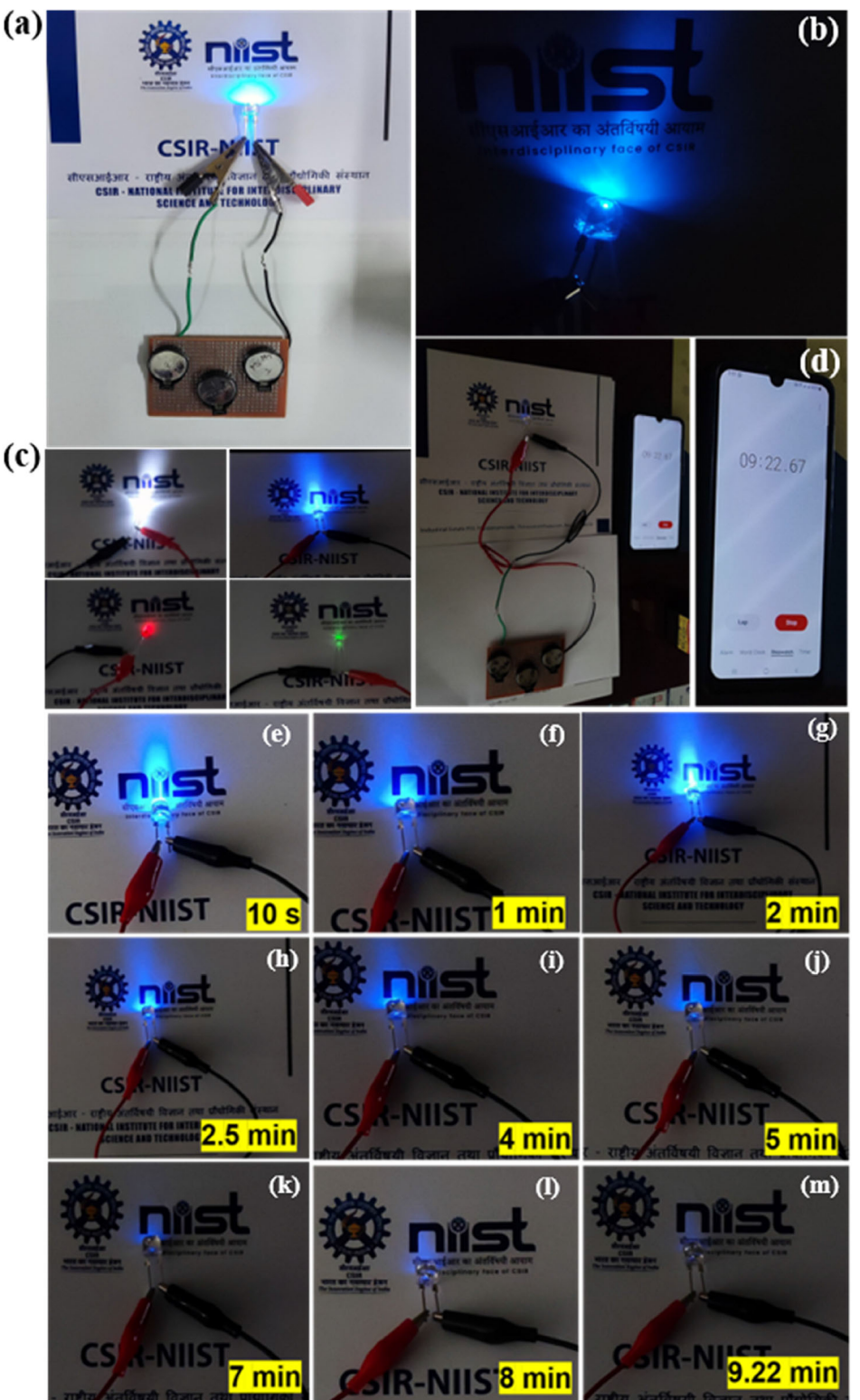


Figure 7. a,c) Cyclic voltammograms and b,d) galvanostatic charge–discharge curves for a single MX-M coin-cell supercapacitor and three MX-M coin-cell supercapacitors connected in series and parallel configurations.

A practical application of the SC device was demonstrated by using it to power LEDs. In the series configuration, three cells charged to 3 V in 10 s using a DC battery were able to power a blue LED with sufficient brightness for 9.22 min and a white

LED for 3 min. Since LEDs are current driven rather than voltage driven, the series configuration provided the required turn-on voltage for the blue LED while maintaining sufficient current density to sustain brightness over an extended period. This device



**Figure 8.** a) Three MX-M coin-cell supercapacitors connected in series to achieve an operating voltage of 4.5 V. b) Optical image of a blue LED powered by the charged MX-M device. c) Optical image of white, blue, red, and green LEDs illuminated by the same cell configuration. d) Timer setup to record the duration of LED illumination. e–m) Sequential images showing the LEDs before they turn off.

demonstrated the ability to power LEDs within the voltage range of 3–5 V, as shown in Figure 8a–c. Four LED colors—white, blue, red, and green were successfully powered by the three-coin-cell series configuration. The voltage output was extended up to a maximum of 4.5 V. Specifically, the blue LED charged for 10 s and sustained illumination for ≈9.22 min, as shown in Figure 8d–m presents sequential images of the LEDs before they turn off. This confirms that the MX–M coin-cell SC device possesses the highest energy-storage capacity, making it a promising candidate for practical applications.

### 3. Conclusion

This study successfully synthesized  $Ti_3C_2T_x$  MXene–TMO-based composites, including MXene–CuO (MX–C), MXene– $Fe_3O_4$  (MX–F), and MXene– $MnO_2$  composites via ultrasonication, leveraging the synergy between MXene and metal oxides to enhance conductivity, ion transport, and electrochemical stability. Among them, MX–M electrodes outperformed MX–C and MX–F within a potential window of 0.8 V in aqueous KOH electrolyte. For real-world applications, the best-performing MX–M electrode was further tested in 1 M  $LiClO_4$ /PC electrolyte, where the resulting MX–M coin-cell SC exhibited a stable operating window of 1.5 V. The device delivered an impressive energy density of  $19.4\text{ Wh kg}^{-1}$  at a power density of  $1.5\text{ kW kg}^{-1}$  and maintained 92% capacitance retention after 10 000 continuous charge–discharge cycles. This study underscores the potential of MXene–TMO composites for high-performance SCs, offering a pathway for developing MXene–TMO-based symmetric devices for practical energy storage.

### 4. Experimental Section

$Ti_3C_2T_x$  MXene layers were synthesized from commercially available titanium aluminum carbide ( $Ti_3AlC_2$ ) MAX phase via a wet chemical etching process using HCl and LiF, as described in our previous work.<sup>[25]</sup> TMO nanoparticles, including CuO,  $Fe_3O_4$ , and  $MnO_2$  with controlled morphologies, were prepared using hydrothermal synthesis. Subsequently,  $Ti_3C_2T_x$ –TMO composites were fabricated through a simple ultrasonication process. Detailed synthesis procedures for all materials are provided in Supporting Information. The electrode materials were analyzed using multiple characterization techniques, including XRD, Raman spectroscopy, FE-SEM, TEM, and BET analysis. XRD was utilized to examine the crystal structure of the samples with an advance powder diffractometer (Bruker D8) using Cu K $\alpha$  radiation of wavelength 1.54 Å. Raman spectroscopy was conducted with a Horiba Micro-Raman spectrometer, employing a 532 nm diode pumped solid state (DPSS) laser source within the spectral range of  $100\text{--}1000\text{ cm}^{-1}$ . The morphological and microstructural features were observed through FE-SEM (Carl Zeiss Sigma) and TEM (Tecnai G2 30 LaB<sub>6</sub> microscope). Furthermore, the specific surface area of the synthesized materials was determined using a Quantachrome Instruments Nova Touch LX4 BET surface analyzer. Electrochemical performance evaluations were conducted using CHI660E and VMP-3 Biologic electrochemical workstation. Electrochemical performance evaluations were conducted using CHI660E and VMP-3 Biologic electrochemical workstations. For the three-electrode configuration, the synthesized material was used as the working electrode, with Ag/AgCl (in saturated KCl) serving as the reference electrode and a platinum wire as the counter

electrode. In the two-electrode setup, the working electrodes were fabricated by drop-coating the active material onto carbon cloth substrates, followed by overnight drying in a vacuum oven to ensure adequate adhesion and removal of any residual solvents. The preliminary two-electrode tests were performed in a standard electrochemical (EL) cell using an aqueous 6 M KOH electrolyte, maintaining a potential window of 0–0.8 V. Based on these results, the highest-performing sample was selected for further testing in a CR2032 coin-cell configuration, utilizing 1 M  $LiClO_4$  in PC organic electrolyte and operating within a potential range of 0–1.5 V. The coin-cell assembly involved stacking the cell components, including the coated electrodes and a Celgard separator soaked in the electrolyte, positioned between the electrodes. The stacked components were subjected to pressure ( $\approx 6900\text{ kPa}$ ) using a crimping machine to improve electrode contact and minimize internal resistance. Once assembled, the coin cell was sealed to prevent electrolyte leakage and contamination from impurities. The coin-cell fabrication process and images of the fabricated cells are presented in Figure S9, Supporting Information.

### Acknowledgements

The author S.M. Varghese is grateful to UGC for senior research fellowship. The author R.B. Rakhi acknowledges financial support from Department of Science & Technology, Ministry of Science & Technology, Government of India (DST/TMD/IC-MAP/2K20/01). The author Srihari R.S. is grateful for the financial support from the DST India's INSPIRE program for research fellowship. The authors are also thankful to Department of Physics, Kariyavattom Campus for Raman Analysis, Dr Subrata Das and Ms. Anjali Santhosh for XRD, Department of Physics, CUSAT for FE-SEM Analysis, Mr. Kiran Mohan for TEM, Mr. Peer Mohammed for BET surface area, Dr. E. Bhoje Gowd, and Ms. Sruthi Suresh for assisting in material synthesis in the initial stage of work.

### Conflict of Interest

The authors declare no conflict of interest.

### Author Contributions

**Radhakrishnan Sheela Srihari:** conceptualization, supervision, validation, resources, funding acquisition, and review and editing of the manuscript. **Moothaveetil Othayoth Anagha:** methodology, investigation, data curation, and formal analysis. **Raghavan Baby Rakhi:** methodology, investigation, data curation, and manuscript editing. **Sophy Mariam Varghese:** conceptualization, methodology, investigation, data curation, formal analysis, and writing—original manuscript draft.

### Data Availability Statement

The data that support the findings of this study are available from the corresponding author upon reasonable request.

**Keywords:** organic electrolytes • specific capacitances • transition metal oxides • wider voltage windows

- [1] Z. W. Seh, K. D. Fredrickson, B. Anasori, J. Kibsgaard, A. L. Strickler, M. R. Lukatskaya, Y. Gogotsi, T. F. Jaramillo, A. Vojvodic, *ACS Energy Lett.* **2016**, *1*, 589.
- [2] S. I. Kim, K. N. Kang, S. W. Kim, J. H. Jang, *RSC Adv.* **2014**, *4*, 59310.
- [3] F. Sharifi, S. Ghobadian, F. R. Cavalcanti, N. Hashemi, *Renewable Sustainable Energy Rev.* **2015**, *52*, 1453.
- [4] J. Wang, S. Kaskel, *J. Mater. Chem.* **2012**, *22*, 23710.
- [5] K. Shi, G. Zhang, Z. Han, L. Ma, J. Hou, D. Song, Z. Fu, W. Zhou, C. Guo, H. Shi, X. Zhu, H. Lan, *Adv. Eng. Mater.* **2024**, *26*, 2301308.
- [6] Y. Sun, G. Shi, *J. Polym. Sci., Part B* **2013**, *51*, 231.
- [7] A. Lipatov, M. Alhabeb, M. R. Lukatskaya, A. Boson, Y. Gogotsi, A. Sinitskii, *Adv. Electron. Mater.* **2016**, *2*, 1600255.
- [8] Y. Dong, S. Zheng, J. Qin, X. Zhao, H. Shi, X. Wang, J. Chen, Z. S. Wu, *ACS Nano* **2018**, *12*, 2381.
- [9] M. Mahmood, A. Rasheed, I. Ayman, T. Rasheed, S. Munir, S. Ajmal, P. O. Agboola, M. F. Warsi, M. Shahid, *Energy Fuels* **2021**, *35*, 3469.
- [10] T. Jiang, Y. Wang, G. Z. Chen, *Small Methods* **2023**, *7*, 2201724.
- [11] S. Nahiriak, A. Ray, B. Saruhan, *Batteries* **2023**, *9*, 126.
- [12] H. Zhou, Y. Lu, F. Wu, L. Fang, H. J. Luo, Y. X. Zhang, M. Zhou, *J. Alloys Compd.* **2019**, *802*, 259.
- [13] B. Aissa, A. Ali, K. A. Mahmoud, T. Haddad, M. Nedil, *Appl. Phys. Lett.* **2016**, *109*, 043109.
- [14] X. Zhang, Z. Zhang, Z. Zhou, *J. Energy Chem.* **2018**, *27*, 73.
- [15] Z. S. Wu, W. Ren, D. W. Wang, F. Li, B. Liu, H. M. Cheng, *ACS Nano* **2010**, *4*, 5835.
- [16] Q. Jiang, N. Kurra, M. Alhabeb, Y. Gogotsi, H. N. Alshareef, *Adv. Energy Mater.* **2018**, *8*, 1703043.
- [17] J. Liu, J. Bao, X. Zhang, Y. Gao, Y. Zhang, L. Liu, Z. Cao, *RSC Adv.* **2022**, *12*, 35556.
- [18] M. Huang, F. Li, F. Dong, Y. X. Zhang, L. L. Zhang, *J. Mater. Chem. A* **2015**, *3*, 21380.
- [19] P. Bhojane, *J. Energy Storage* **2022**, *45*, 103654.
- [20] D. V. Rupnar, S. A. Mane, H. Razi, V. H. Goswami, B. G. Pawar, P. B. Sarwade, N. S. Ramgir, *Inorg. Chem. Commun.* **2025**, *173*, 113784.
- [21] S. N. Ansari, M. Saraf, Z. Abbas, S. M. Mobin, *Nanoscale* **2023**, *15*, 13546.
- [22] A. D. Rajeeve, R. Yamuna, M. Vinoba, M. Bhagiyalakshmi, *Langmuir* **2023**, *39*, 17688.
- [23] W. Liang, I. Zhitomirsky, *Materials* **2021**, *14*, 2930.
- [24] L. Zhang, Z. Wang, W. Chen, R. Yuan, K. Zhan, M. Zhu, J. Yang, B. Zhao, *Nanoscale* **2021**, *13*, 15343.
- [25] Q. Wang, Z. Zhang, Z. Zhang, X. Zhou, G. Ma, *J. Solid State Electrochem.* **2019**, *23*, 361.
- [26] Y. Tang, J. Zhu, C. Yang, F. Wang, *J. Alloys Compd.* **2016**, *685*, 194.
- [27] R. B. Rakhi, B. Ahmed, D. Anjum, H. N. Alshareef, *ACS Appl. Mater. Interfaces* **2016**, *8*, 18806.
- [28] S. D. Raut, H. R. Mane, N. M. Shinde, D. Lee, S. F. Shaikh, K. H. Kim, H. J. Kim, A. M. Al-Enizi, R. S. Mane, *New J. Chem.* **2020**, *44*, 17864.
- [29] X. Wang, Y. Zhou, *J. Mater. Chem.* **2002**, *12*, 455.
- [30] X. Li, G. Fan, C. Zeng, *Int. J. Hydrogen Energy* **2014**, *39*, 14927.
- [31] E. Mitchell, R. K. Gupta, K. Mensah-Darkwa, D. Kumar, K. Ramasamy, B. K. Gupta, P. Kahol, *New J. Chem.* **2014**, *38*, 4344.
- [32] Y. Wang, Y. Li, Z. Qiu, X. Wu, P. Zhou, T. Zhou, J. Zhao, Z. Miao, J. Zhou, S. Zhuo, *J. Mater. Chem. A* **2018**, *6*, 11189.
- [33] W. Chen, R. B. Rakhi, Q. Wang, M. N. Hedhili, H. N. Alshareef, *Adv. Funct. Mater.* **2014**, *24*, 3130.
- [34] S. M. Varghese, V. V. Mohan, S. Suresh, E. Bhoje Gowd, R. B. Rakhi, *J. Alloys Compd.* **2024**, *973*, 172923.
- [35] J. Yan, C. E. Ren, K. Maleski, C. B. Hatter, B. Anasori, P. Urbankowski, A. Sarycheva, Y. Gogotsi, *Adv. Funct. Mater.* **2017**, *27*, 1701264.
- [36] Q. Liu, J. Yang, X. Luo, Y. Miao, Y. Zhang, W. Xu, L. Yang, Y. Liang, W. Weng, M. Zhu, *Ceram. Int.* **2020**, *46*, 11874.
- [37] K. Sahu, B. Satpati, S. Mohapatra, *Appl. Phys. A* **2021**, *127*, 361.
- [38] R. Kumar, R. K. Singh, A. R. Vaz, R. Savu, S. A. Moshkalev, *ACS Appl. Mater. Interfaces* **2017**, *9*, 8880.
- [39] M. Wei, Y. Konishi, H. Zhou, H. Sugihara, H. Arakawa, *Nanotechnology* **2005**, *16*, 245.
- [40] J. E. Post, D. A. McKeown, P. J. Heaney, *Am. Mineral.* **2020**, *105*, 1175.
- [41] R. B. Rakhi, W. Chen, D. Cha, H. N. Alshareef, *J. Mater. Chem.* **2011**, *21*, 16197.
- [42] Y. Tang, C. Yang, W. Que, *J. Adv. Dielectr.* **2018**, *8*, 1850035.
- [43] A. Hermawan, B. Zhang, A. Taufik, Y. Asakura, T. Hasegawa, J. Zhu, P. Shi, S. Yin, *ACS Appl. Nano Mater.* **2020**, *3*, 4755.
- [44] C. K. Kamaja, S. Mitra, M. Katiyar, *Energy Fuels* **2022**, *36*, 703.
- [45] Y. Zhang, X. Li, W. Xi, Q. Zhang, X. Ge, J. You, Q. Zhang, D. Shi, J. Jin, *Chem. Synth.* **2024**, *4*, 19.
- [46] A. M. Aravind, M. Tomy, A. Kuttapan, A. M. Kakkassery Aippunny, X. T. Suryabai, *ACS Omega* **2023**, *8*, 44375.
- [47] D. Zhang, J. Yang, J. Li, *Vacuum* **2020**, *109455*.
- [48] D. Wen, G. Ying, L. Liu, C. Sun, Y. Li, Y. Zhao, Z. Ji, Y. Wu, J. Zhang, J. Zhang, X. Wang, *Adv. Mater. Interfaces* **2021**, *8*, 2101453.
- [49] C. An, Y. Zhang, H. Guo, Y. Wang, *Nanoscale Adv.* **2019**, *1*, 4644.
- [50] C. Xiong, Y. Su, *Adv. Sustainable Syst.* **2024**, *8*, 2400578.
- [51] T. S. Mathis, N. Kurra, X. Wang, D. Pinto, P. Simon, Y. Gogotsi, *Adv. Energy Mater.* **2019**, *9*, 1902007.
- [52] X. Zhang, B. Shao, A. Guo, Z. Sun, J. Zhao, F. Cui, X. Yang, *Appl. Surf. Sci.* **2021**, *560*, 150040.
- [53] S. Chen, Y. Xiang, W. Xu, C. Peng, *Inorg. Chem. Front.* **2019**, *6*, 199.
- [54] M. Zhu, Y. Yang, *New J. Chem.* **2025**, *49*, 5565.
- [55] T. Arun, A. Mohanty, A. Rosenkranz, B. Wang, J. Yu, M. J. Morel, R. Udayabhaskar, S. A. Hevia, A. Akbari-Fakhrebadi, R. V. Mangalaraja, A. Ramadoss, *Electrochim. Acta* **2021**, *367*, 137473.
- [56] H. Jiang, Z. Wang, Q. Yang, M. Hanif, Z. Wang, L. Dong, M. Dong, *Electrochim. Acta* **2018**, *290*, 695.
- [57] Y. Zhu, K. Rajouà, S. Le Vot, O. Fontaine, P. Simon, F. Favier, *J. Electrochem. Soc.* **2022**, *169*, 030524.
- [58] H. Zhou, Y. Lu, F. Wu, L. Fang, H. Luo, Y. Zhang, M. Zhou, *J. Alloys Compd.* **2019**, *802*, 259.
- [59] W. Yuan, L. Cheng, B. Zhang, H. Wu, *Ceram. Int.* **2018**, *44*, 17539.
- [60] Z. Sun, H. Xu, J. Fu, H. Bai, Y. Qiao, P. Liu, Y. Li, Y. Jiang, B. Hou, Y. Wang, *Sep. Purif. Technol.* **2024**, *347*, 127520.

Manuscript received: April 23, 2025

Revised manuscript received: June 2, 2025

Version of record online: